Materials Horizons

ROYAL SOCIETY OF CHEMISTRY

COMMUNICATION

View Article Online
View Journal | View Issue

Cite this: *Mater. Horiz.*, 2022, 9, 1690

Received 3rd March 2022,
Accepted 22nd March 2022

DOI: 10.1039/d2mh00276k

rsc.li/materials-horizons

A thermally conductive interface material with tremendous and reversible surface adhesion promises durable cross-interface heat conduction†

Cong Guo,[a] Yuhan Li,[b] JianHua Xu,[c] Qin Zhang,[a] Kai Wu *[a] and Qiang Fu *[a]

The dramatic miniaturization and integration of electronic devices call for next-generation thermally conductive interface materials with higher service performance and long-term stability. In addition to enhancing the inherent thermal conductivity of materials, it is noteworthy to pay attention to the thermal contact resistance. Herein, we synthesized a polyurethane with hierarchical hydrogen bonding to realize high surface adhesion with substrates; another key was incorporating aluminum oxide modified by a deformable liquid metal to improve the thermo-conductive capability and offer the freedom of polymeric segmental motions. These molecular and structural designs endow the composite with high isotropic thermal conductivity, electrical insulation and temperature-responsive reversible adhesion, which enable low thermal resistance and durable thermal contact with substrates without the need for external pressure.

New concepts

Traditional methods employ thermal interface materials (TIMs) with high thermal conductivity and geometric adaptation to facilitate cross-interface thermal transport. However, they require external packing pressure and still suffer from deteriorated thermal contact resistance during long-term service, attributed to their thermal expansion coefficient mismatch with the target substrates. Herein, we propose a new concept of building reversible binding moieties on highly thermo-conductive yet electrically insulating TIMs to guarantee zero packing pressure and enduring interfacial adaptation. We synthesize a ternary polyurethane/liquid metal (LM)/aluminum oxide (Al_2O_3) composite as a proof-of-concept. Polyurethane consists of macromolecular chains carrying abundant hierarchical hydrogen bonds, and the LM is exquisitely engineered at the polymer–Al_2O_3 interface. The former molecular design guarantees dynamic hydrogen bonds with target substrates beyond mere conformable contact. The latter filler modification balances the dilemma that high thermal conductivity through adding rigid filler contradicts the reversibility of high surface adhesion. Specifically, adjacent Al_2O_3 particles are bridged *via* the interconnection of liquid metal droplets; the introduction of liquid metal also offers the freedom of polymeric segmental motions for reversible interfacial bindings. As a result, these intrinsic features promise a zero-pressure-packing interface with an ignorable increment in thermal contact resistance after 7500 times of cyclic heating and cooling.

1 Introduction

As electronic devices develop towards high frequency, high power density, multi-functionalization, and miniaturization, exponentially increasing heat has become a dominant issue for operating performance, reliability, and lifespan. State-of-the-art heat-dissipation materials and techniques have attracted increasing attention.[1–4] In particular, when heat passes through a macro interface between the heat source and heat sink, air grooves and valleys resulting from imperfect interfacial contact will seriously impede thermal transport. This becomes one of the bottleneck problems for electronic thermal management. Current engineering strategies usually employ a thermal interface material (TIM) to boost the interfacial heat conduction, and a parameter named thermal interfacial resistance (R_i) usually describes its thermal-management efficiency, according to eqn (1):

$$R_i = \frac{\mathrm{BLT}}{\kappa} + R_{c1} + R_{c2} \quad (1)$$

where κ is the thermal conductivity of the TIM, BLT is the bond line thickness, and R_{c1} and R_{c2} represent the thermal contact resistance (R_c) values between the TIM and the double surfaces. Recently, most efforts have been devoted to enhancing the inherent κ of TIMs.[5–17] Typically, a distinctive thermo-conductive filler, gallium-based liquid mental (LM), combining the deformation ability of a liquid and high thermal conductivity (39 W m^{-1} K^{-1}) of a metal, has received extensive attention in soft polymer-based thermally conductive composites.[18–20] For example, an LM–methyl silicon oil

[a] College of Polymer Science and Engineering, State Key Laboratory of Polymer Materials Engineering, Sichuan University, Chengdu 610065, P. R. China. E-mail: kaiwu@scu.edu.cn, qiangfu@scu.edu.cn
[b] College of Chemistry and Green Catalysis Center, Zhengzhou Key Laboratory of Elastic Sealing Materials, Zhengzhou University, Zhengzhou 450001, China
[c] Joint Laboratory of Advanced Biomedical Materials, College of Chemical Engineering, Nanjing Forestry University, Nanjing 210037, P. R. China

† Electronic supplementary information (ESI) available. See https://doi.org/10.1039/d2mh00276k

composite was reported to achieve a unique combination of high thermal conductivity (5.27 W m^{-1} K^{-1}), high electrical resistance, excellent wettability and compliance during application.[21] This combination of soft merits but high thermal conductivity has rarely been found in other polymer/filler composites. After the continuous efforts recently, researchers further developed LM–polymer composites with higher thermal conductivity and multifunctional properties,[22–25] by regulating the morphology of LM droplets or employing other hybrid fillers.[26,27] However, although high thermal conductivities could be realized in such previous solid-state examples, the efficient cross-interface heat conduction is still hampered due to the troublesome R_c. For example, a graphene/silicon carbide hybrid paper manifests a through-plane thermal conductivity ($\kappa_\perp$) of up to 17.6 W m K^{-1}. When it is applied as a TIM for dissipating heat in electronic components, the effective thermal conductivity of the sandwiched interface deteriorates to only 4.1 W m K^{-1}.[28] Furthermore, it is assumed that when the TIM thickness is reduced to be smaller than 50 μm, R_c will occupy more than 50% of the total thermal interfacial resistance, even dominating the cross-interface thermal transport. This predicament puts urgent requirements for rational interfacial engineering strategies for a significant R_c reduction, beyond the mere achievement of high thermal conductivity.

One approach to the above issue of R_c is controlling the TIMs in the form of thixotropic gels or flowable liquids, which integrates both high κ and stereo conformable advantages. For instance, commercial thermal grease, thermal gel, or phase-change TIMs with responsive liquidity could adequately fill the interstitial gap with suitable pressures, presenting a much lower R_c and thus a total thermal interfacial resistance of only 20–100 mm^2 K W^{-1}.[29] A solid-state thermal pad is more popular regarding thermal interfaces with larger air gaps. Traditional methods regarding the thermal pad mitigate R_c primarily *via* minimizing the elastic modulus (<2 MPa for conventional TIMs) or applying high pressure to the sandwiched thermal interface. For example, a 500 kPa pressure was employed onto a panel-like graphene thermal pad when it was packed between a heater and heat sink, which can give rise to a 248% decrease of R_c in comparison with applying an 81 kPa pressure.[30] However, high pressure destroys parts of electronic devices and increases complications in actual applications, restricting applications in electronics vulnerable to external forces.[31] More than forming conformable contacts with double sides of the interface by applying a high packing pressure, the past two decades have also witnessed tremendous achievements in understanding the interfacial heat conduction in the nano- or micro-scale. They suggest that interface adhesion and a molecular bridge will make interfacial adaption easier under much lower packing pressure and significantly contribute to interfacial thermal transport.[32–34] For example, high interfacial bindings with the double surfaces through metallization, covalent bonds, or non-covalent interactions demonstrate a more reliable thermal boundary conductance.[35–39] The robust interfacial interactions will also open up opportunities for credible out-of-plane conduction when the electronics are exposed to repeated bending, twisting, and stretching, which may be essential in potential applications of the next-generation soft and stretchable electronic devices. However, concerning current TIMs, high interfacial binding is seldom implemented to reduce R_c, and their relationship lacks systematic research. Another formidable challenge is that the stereo adaptation by applying pressures or chemical adhesion in current TIMs is very vulnerable to cyclic heating and cooling. The thermal expansion coefficient mismatch with some target substrates (*i.e.*, metals, ceramics) leads to deteriorated geometric adaptation or interfacial debonding, which increases the R_c and seriously affects the ability of TIMs to serve in the long term.[29]

In this study, we synthesized a ternary polyurethane with 2,6-pyridinedimethanol as a chain extender (PUPDM)/liquid metal (LM)/aluminum oxide (Al_2O_3) composite with inherently high thermal conductivity and dynamic hydrogen bonds. The former high κ furnishes efficient out-of-plane thermal transport within the PUPDM/LM/Al_2O_3 TIM. Simultaneously, the latter dynamic bonds are expected to release hydrogen bonding moieties reversibly to offer a durable adhesion force with target objects under minimal pressure to overcome the interfacial debonding and geometric mismatch in long-term service. However, the challenge is to balance the dilemma that electrically insulating high κ by adding great ceramic fillers contradicts the reversible nature of high adhesion strength, since the high content of phonon-based filler will weaken the dynamics of hydrogen bonds and diffusion kinetics of PUPDM chains. Inspired by the fact that a soft liquid could release the freedom of macromolecular movements in a polymer composite, we localized one type of thermo-conductive and deformable LM droplet partially at the PUPDM-rigid Al_2O_3 interface. These engineered liquid droplets not only bridge adjacent Al_2O_3 particles to form synergistic thermal pathways but also vastly reduce the internal friction of PUPDM segmental motions. Compared to the counterpart employing pure Al_2O_3, the exquisite PUPDM/LM/Al_2O_3 composite manifests a 2.58-fold κ, together with a segmental relaxation time of only 1.27 s at 40 °C. As a result, for the first time under zero pressure, valid and durable heat conduction passing through a macro thermal interface is achieved by applying our TIM, with a meager R_c value of only 18.28 mm^2 K W^{-1}. This zero-pressure-packing R_c has never been reported in previous studies reported in the literature. More importantly, this reversibly bonded thermal interface demonstrates a minimal R_c increment after 7500 cyclic heating and cooling cycles. However, for the other ones applying a commercial adhesive thermal pad or flowable thermal grease, the R_c value deteriorates to 750% or 415%, respectively. These findings are inspiring, and this concept of building dynamic and reversible bindings at the thermal interface is believed to be instructive for new thermal-management materials and techniques.

2 Results and discussion

2.1 Molecular and structural design

The reversibly adhesive PUPDM was synthesized by a two-step prepolymer method. Polytetramethylene ether glycol (PTMEG)

was used as a soft segment, isophorone diisocyanate (IPDI) as a hard segment, and 2,6-pyridinedimethanol (PDM) as a chain extender. PTMEG, a polyol with a linear structure and suitable effective length, could provide the resultant elastomer with good flexibility, softness, and segmental mobility due to the favorable rearrangement of the chain conformation and alignment of soft segments under external force. The experimental section gives the synthesis details. ^{1}H nuclear magnetic resonance, Fourier transform- infrared (FTIR) spectroscopy, and gel permeation chromatography demonstrate the successful synthesis of PUPDM (Fig. S2 and Table S3, ESI†). As shown in Fig. 1a-(i), we expect two hierarchical hydrogen bonding moieties (*i.e.*, carbamate and pyridine) in the PUPDM chain to provide improved strength and adequate adhesion with the target heat sink and heat source (*e.g.*, metals, polymers, or ceramics). At the same time, the asymmetric alicyclic structure of IPDI gives rise to loosely-packed configurations in hard domains. It thus promotes the dynamic nature and reversibility of the interfacial bindings when sandwiched between a thermal interface.[40] As shown in Fig. S3 (ESI†), the carbamate–carbamate and carbamate–pyridine hydrogen bonds within the PUPDM network are proved to be temperature-responsive. Specifically, the hydrogen bonding moieties are released at high temperatures to provide active binding sites with the hydrogen bond acceptor or donor on the sandwiched surfaces, promising high adhesion force.[41–43] Meanwhile, the association and disassociation processes of the hydrogen bonds are dynamic and reversible when the specimen is heated and cooled repeatedly. This will open opportunities for reversible and robust adhesion with the targets. The high adhesion force was verified by the lap-shear strength tests, in which the pristine PUPDM sample was glued by two substrates followed by exerting a preload at a certain temperature before conducting the mechanical test (Fig. S4a, ESI†). The adhesive property could be optimized by tuning the value of NCO/OH, which could alter the total content of the hard segments. The adhesion force of PUPDM with a NCO/OH value of 2.7 is the highest (Fig. S4b, ESI†), so we selected PUPDM with a NCO/OH value of 2.7 as the object of the following study and matrix of the composites. Fig. 1b and Fig. S4c (ESI†), show the adhesion force of

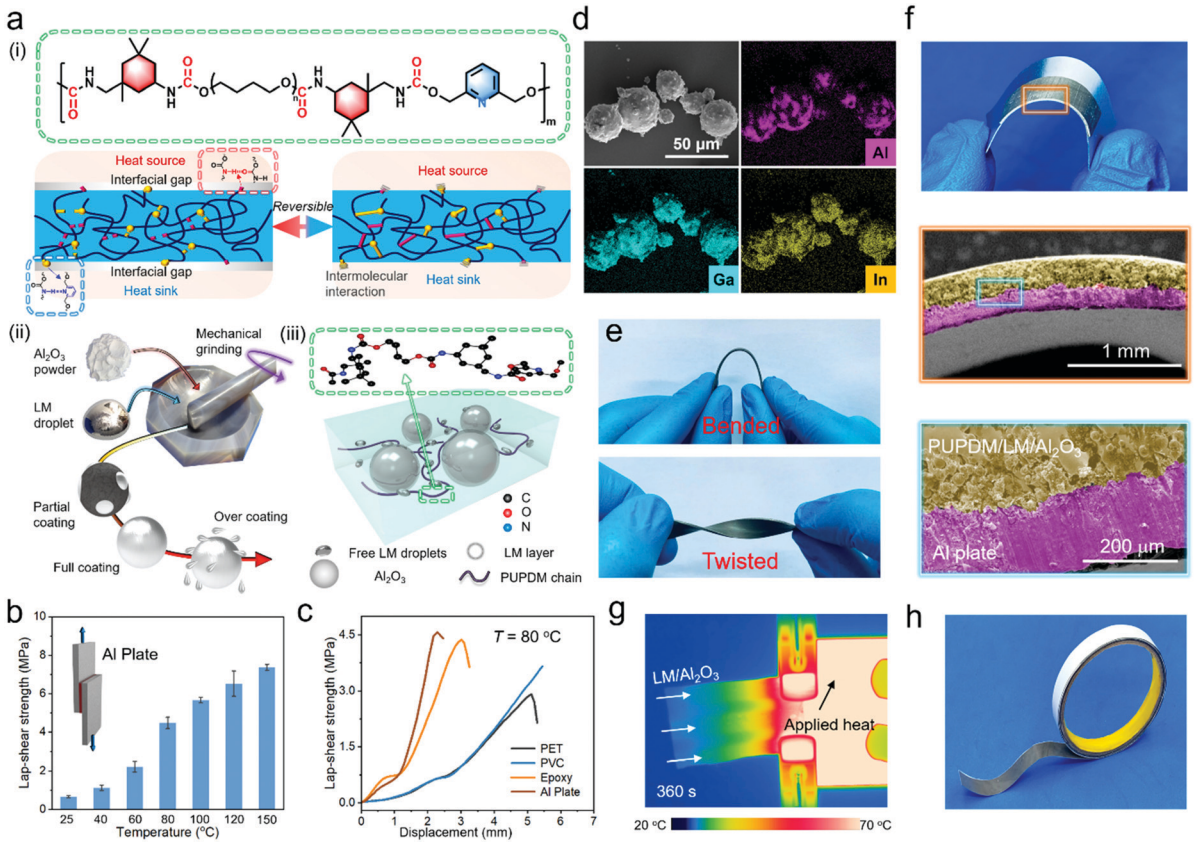

Fig. 1 Molecular and structural design of the PUPDM composite. (a) The fabrication of the PUPDM/LM/Al_2O_3 composite involves three procedures: (i) chemical design and experimental synthesis of a PUPDM with hierarchical hydrogen bonds and its temperature-responsive reversible adhesion with different substrates; (ii) fabrication of the core–shell LM/Al_2O_3 filler *via* a grinding method; (iii) direct mixing of PUPDM and core–shell LM/Al_2O_3 into the PUPDM/LM/Al_2O_3 composites. (b) Lap-shear strength of pristine PUPDM between two glued aluminum plates at different adhesion temperatures. (c) Lap-shear strength *versus* displacement curves of pristine PUPDM between various glued plates at the adhesive temperature of 80 °C. (d) Scanning electronic macroscopy mapping results of the LM/Al_2O_3 filler manifesting its core–shell morphology. (e) Photographs demonstrating the flexibility of the PUPDM/LM/Al_2O_3 composite (LM/Al_2O_3 content is 73.68 vol%). (f) Photograph and cross-sectional scanning electronic microscopy images exhibiting remarkable adhesion on an aluminum plate. (g) Infrared camera image of alternating strips of the PUPDM/LM/Al_2O_3 composite and PUPDM showing the high thermo-conductive property of the PUPDM/LM/Al_2O_3 composite. (h) Photograph showing that the PUPDM/LM-Al_2O_3 composite can be tailored into a hot-melt adhesive tape.

PUPDM at different temperatures and the solid-state PUPDM adhered at 80 °C manifests a lap-shear strength reaching 4.48 MPa when two aluminum plates sandwich it. This value further increases to 7.36 MPa when the adherence temperature exceeds 120 °C. Apart from the aluminum plate, other plastic and thermoset substrates integrated with our PUPDM also show high lap-shear strength (Fig. 1c and Fig. S4d, ESI†), including the substrates made of polyethylene terephthalate (PET), polyvinyl chloride (PVC), and epoxy. Therefore, unlike traditional thermoset TIMs providing non-dynamic interfacial bindings, this high adhesion ability offered by the dynamic and reversible hydrogen bonds may effectively prevent the PUPDM from geometric interface mismatch during long-term service. Our artificial PUPDM is considered a promising candidate in applications as a state-of-the-art TIM polymer matrix.

For a significant κ improvement, a core–shell hybrid filler (LM/Al_2O_3) with theoretical isotropic thermal conductivity was employed to prepare the TIM. The LM we used was galinstan that comprises 78.3% at% Ga, 14.9 at% In and 6.8 at% Sn, and the melting temperature was 13.2 °C. The spherical Al_2O_3 was selected due to its isotropic thermo-conductive trait, which enables the resultant composites to realize effective thermal management of not only a spot-like heat source but also a large-area heat source.[44] Rather than directly compositing LM and Al_2O_3 with the PUPDM independently, LM droplets were firstly ground with Al_2O_3 particles using an agate mortar to form the homogeneous hybrid (Fig. 1a-(ii, iii) and Fig. S5, ESI†). During the mechanical grinding process, the lone pair of electrons outside O atoms (Al_2O_3) will enter the empty orbitals of Ga, In, and Sn atoms (LM), leading to the formation of coordination bonds at the heterogeneous interface, and meanwhile, turning the hybrid filler into a core–shell morphology depending on the LM volume fraction (Fig. 1d and Fig. S6a, b, S7, ESI†). The X-ray diffraction result manifests a gradual shift of a crystalline peak at $\approx 32.9^\circ$ (Fig. S6c and d, ESI†), indicating that some Ga/In/Sn atoms may propagate into the lattice of Al_2O_3 to distort the crystal lattice. As a result, this core–shell LM/Al_2O_3 could be very stable under various polymer processing fields (*e.g.*, sonication, stirring, and turbulent flow), keeping the LM shell anchored on the Al_2O_3 core (Fig. S6e, ESI†). This core–shell structure is particularly advantageous. Firstly, the liquid shell of LM/Al_2O_3 is mergeable and inherently thermo-conductive,[18,19] which may facilitate the formation of the continuous thermal pathways at the high filler contents where filler–filler contact frequently exists. Secondly, LM is soft and deformable, which will relieve the adverse effects of the rigid Al_2O_3 in hardening the PUPDM composite and limiting the segmental motion of the polymer matrix.

After solution-mixing the LM/Al_2O_3 binary filler into the PUPDM solution and processing them into the solid-state composite (thickness >100 μm) by hot-pressing by virtue of the thermoplastic nature of PUPDM (Fig. S8 and S9, ESI†), the $PUPDM/LM/Al_2O_3$ composite exhibits many prominent properties. For example, even at a high filler content (73.68 vol% LM/Al_2O_3), this PUPDM composite still makes repeat bending and twisting operational without any mechanical destruction, manifesting its good flexibility and softness (Fig. 1e). It could

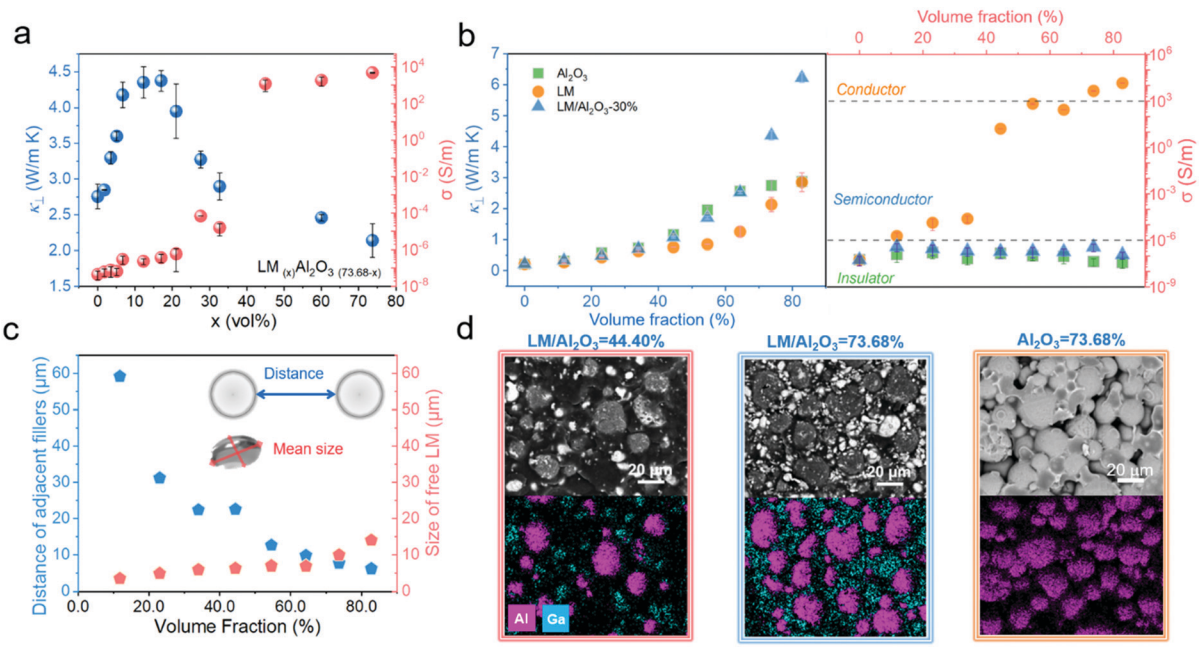

Fig. 2 Thermally conductive yet electrically insulating properties of the PUPDM composite. (a) Thermal conductivity and electrical conductivity of the $PUPDM/LM/Al_2O_3$ composite as a function of the LM/Al_2O_3 volume ratio. Note that the total volume content of the binary filler is 73.68%. (b) Out-of-plane thermal and electrical conductivity as a function of the volume fraction of the binary filler for different PUPDM composites. Note that the LM/Al_2O_3 volume ratio is 30%. (c) Average distance between adjacent fillers and an average size of the free LM as a function of the volume fraction of the binary filler in the $PUPDM/LM/Al_2O_3$ composite. (d) Scanning electron microscopy images and the elemental mapping images of the $PUPDM/LM/Al_2O_3$ and $PUPDM/Al_2O_3$ composites.

adhere to versatile substrates, for example, aluminum plates and when the sandwiched sample is bent, the interfacial bindings are preserved without any visual air grooves and valleys (Fig. 1f). Moreover, equipped with an infrared thermal imaging technology, much efficient heat conduction was observed in this PUPDM composite compared with that of the pristine PUPDM material (Fig. 1g), demonstrating its high thermal conductivity. More importantly, our PUPDM/LM/Al_2O_3 adhesive can provide good scalability. As depicted in Fig. 1h, it could be customized into sundry product shapes through a simple molding processing method, such as a hot-melt adhesive tape allowing high convenience in handling the thermal interface.

2.2 Thermo-conductive yet electrically insulating performance

Laser flash analysis was used to investigate the thermal conductivity that dictates the heat flux within the TIM of a sandwiched thermal interface. Fig. 2a plots the κ and electrical conductivity (σ) of the PUPDM/LM/Al_2O_3 composites as a function of the volume ratio of LM : Al_2O_3. At a constant filler content (*e.g.*, 73.68 vol%), the PUPDM composite with a volume ratio (LM : Al_2O_3) of 30% sshows the highest κ, while the σ is still maintained in the range of an insulator, which indicates that 30% is an optimized volume ratio for this binary filler in enhancing the electrically insulating κ. Based on this result, the κ and σ of the PUPDM/LM/Al_2O_3 composites were further studied as a function of the total filler volume content, as the volume ratio of LM : Al_2O_3 was maintained at 30%. In Fig. 2b, the pristine PUPDM shows a κ of only 0.22 W m^{-1} K^{-1}, while the PUPDM/LM/Al_2O_3 composite property reaches as high as 6.23 W m^{-1} K^{-1} at an 82.76 vol% content. At such a high filler loading, the ternary composite is still a good insulator. Because the main constituent of the binary hybrid filler, aluminum oxide, is inherently electrically insulating, it impedes the formation of an electrically percolated LM network at such a filler content. However, the PUPDM counterpart employing the same volume fraction of Al_2O_3 shows a κ of only 2.88 W m^{-1} K^{-1}, while another employing the LM shows a percolated σ of 14 625 S m^{-1}.

The 2.16-fold κ and its insulting behaviour result from the exquisite manipulation of the LM distribution in the PUPDM matrix. Typically, the surface of Al_2O_3 is entirely covered by the liquid LM at a 30% volume ratio of LM : Al_2O_3 (Fig. S6a, ESI†). After being introduced into the matrix, LM falls partially from the Al_2O_3 particles due to the intense shearing during the physical mixing process. These LM droplets will be free as merged agglomerations within the composite. Note that the LM/Al_2O_3 binary fillers and free LM both disperse in the matrix uniformly even at high filler loadings, instead of displaying an obvious gradient distribution, proving no precipitation of LM in the composites (Fig. S10, ESI†). As the total filler content increased, we found that the distance between two adjacent LM/Al_2O_3 particles decreased, and the average diameter size of the free LM droplets increased (Fig. 2c and Fig. S10, ESI†). As the filler volume fraction approaches 64.30%, the former is almost the same as the latter, where the free LM droplets will connect the adjacent LM/Al_2O_3 particles and promote the formation of more continuous thermal pathways (Fig. S11, ESI†). The scanning electron microscopy (SEM) elemental mapping results further verified the bridging effect. The regions among adjacent LM/Al_2O_3 particles (Al element) have been wholly occupied by the free LM droplets (Ga element) when the volume fraction of the binary filler exceeds 64.30% (Fig. 2d). Therefore, compared to employing merely one kind of thermo-conductive filler, this core–shell binary filler shows a remarkable synergistic effect in enhancing the thermal conductivity. Its synergy achieves as high as 237% (Fig. S12, ESI†), outperforming those of the most reported synergistic methods *via* employing double fillers,[6,15,45–48] and we have qualified the synergy in Fig. S13 (ESI†) by fitting the microscopic interfacial thermal resistance between thermo-conductive fillers and the PUPDM matrix based on the effective medium theory (ESI†),[49] which is an important parameter reflecting the efficiency of the thermal pathways. Moreover, both the thermo-conductive traits of LM and Al_2O_3 are isotropic. Therefore, the PUPDM composite employing this kind of binary filler behaves with isotropic thermal conductivities (Fig. S14, ESI†), which is particularly beneficial for thermal management of spot-like and large-area heat sources (Fig. S15 and S16, ESI†).[44]

2.3 Dynamic and reversible adhesive performance

For the PUPDM/LM/Al_2O_3 composite, the reversible adhesion force depends on the PUPDM chain diffusion and the association and dissociation kinetics of the hydrogen bonds. However, they contradict the high thermal conductivity because the employed high-κ fillers will exacerbate the internal friction of the molecular chain and impede its effective segmental motions. In Fig. 3a, a relaxation test was carried out to investigate the chain dynamics of the pristine PUPDM, PUPDM/LM, PUPDM/Al_2O_3, and PUPDM/LM/Al_2O_3 composites, respectively. As shown, the relaxation time (τ) of the pure PUPDM is 44.45 s at 40 °C. However, as the temperature increases up to 80 °C, the τ value further decreases to 2.17 s, demonstrating the faster chain dynamics at high temperatures (Fig. 3b). Once the rigid Al_2O_3 is incorporated into the PUPDM matrix, the segmental motions of macromolecular PUPDM are obstructed as the relaxation time of the PUPDM/Al_2O_3 composite increases to 89.83 s and 6.40 s at 40 °C and 80 °C, respectively. In sharp contrast, the soft and deformable LM is found to be adequate to encourage the segmental movements in the composite, as the relaxation time of the PUPDM/LM composite is much lower. More interestingly, when the LM droplets are partially coated on the Al_2O_3, the relaxation time of the PUPDM/LM/Al_2O_3 composite stepwise decreases as compared to that of the PUPDM/LM composite. We speculate that the mediate LM droplets on the surface of Al_2O_3 show a higher specific surface than being agglomerated as larger droplets within the PUPDM/LM composite, which releases more freedom for interfacial PUPDM segments to vibrate and rotate. Subsequently, the Arrhenius function was employed to fit the activation energy (E_a) for the mobility of the polymer chains (Fig. 3c and Fig. S17, ESI†). As shown, the PUPDM/LM/Al_2O_3 composite behaves with the lowest activation energy. The coated and free LM droplets are expected to

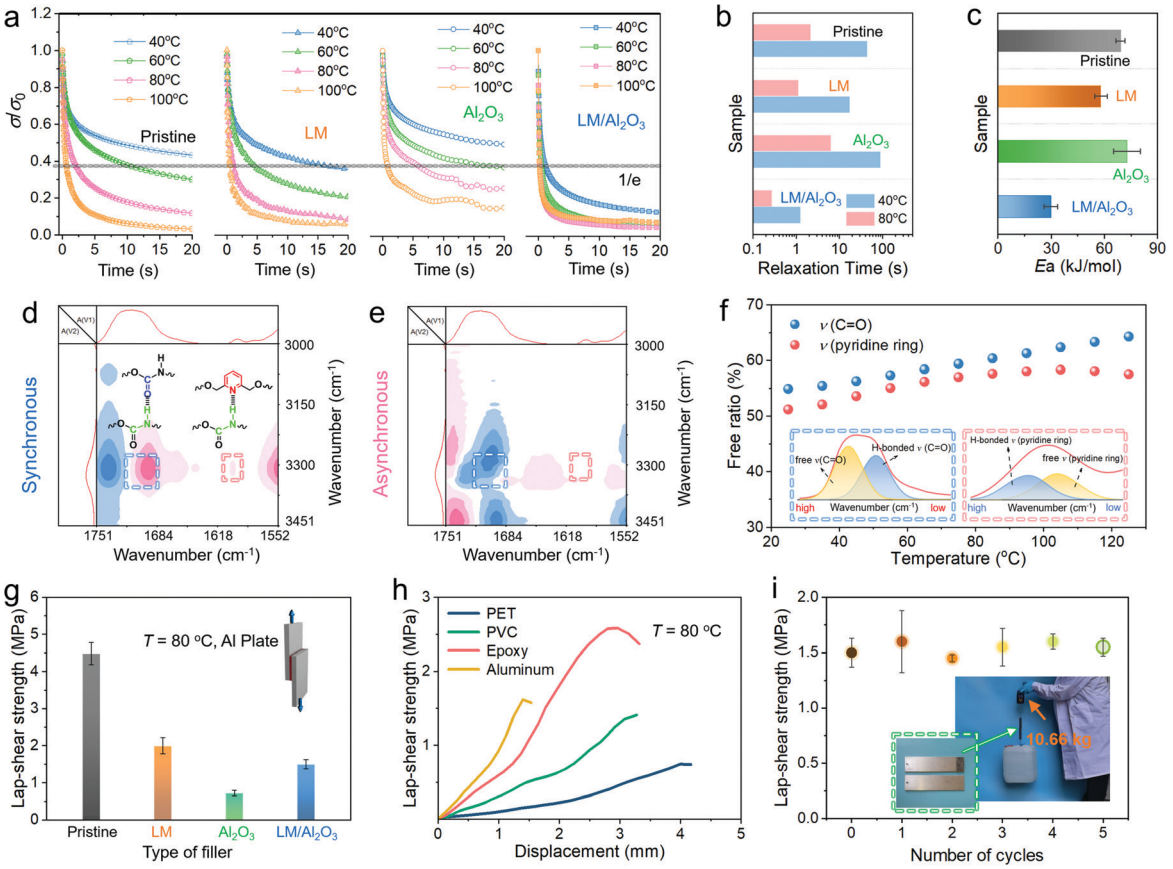

Fig. 3 Dynamic and reversible adhesive performance of the PUPDM composites. (a) Stress relaxation curves of pristine PUPDM, PUPDM/LM, PUPDM/Al_2O_3, and PUPDM/LM/Al_2O_3 composites at different temperatures. The filler content in the composites is constant at 73.68 vol%. σ and σ_0 mean the real-time shear stress and the initial shear stress, respectively. (b) Relaxation times and (c) activation energies of the pristine PUPDM, PUPDM/LM, PUPDM/Al_2O_3, and PUPDM/LM/Al_2O_3 composites. (d) Synchronous and (e) asynchronous two-dimensional Fourier transform infrared spectrum results of the PUPDM/LM/Al_2O_3 composite. (f) Percentage of free carbamate and pyridine hydrogen bonding moieties derived from the Fourier transform infrared spectrum of the PUPDM/LM/Al_2O_3 composite. Inset two images show the typical calculation details *via* means of peak separation. (g) Lap-shear strength of the pristine PUPDM, PUPDM/LM, PUPDM/Al_2O_3, and PUPDM/LM/Al_2O_3 composites in gluing aluminum plates, attached at 80 °C. (h) Lap-shear strength *versus* displacement curves of the PUPDM/LM/Al_2O_3 composite in gluing different substrates adhered at 80 °C. (i) Lap-shear strength of the PUPDM/LM/Al_2O_3 composite in gluing aluminum plates at 80 °C after different numbers of cyclic adhesion and debonding. The inset image shows a 10.66 kg bucket lifted by the PUPDM/LM/Al_2O_3 composite bonded aluminum sheets.

provide high freedom for the diffusion of chain segments, which promise more possibilities for the hydrogen bonding moieties to interact with the double sides of the sandwiched interface.

The dynamic abilities of the carbamate–carbamate and pyridine–carbamate hydrogen bonds within the PUPDM/LM/Al_2O_3 network were validated by 2D-correlation FTIR (Fig. 4d and e), which is calculated based on temperature-dependent FTIR (Fig. S18, ESI†). The PUPDM/LM/Al_2O_3 composite shares the same carbamate–carbamate and pyridine–carbamate hydrogen bonds as that in pristine PUPDM. More importantly, these hydrogen bonds are still dynamic, even at such a high filler content. Specifically, the FTIR absorption regions of $\nu_{C=O}$ and $\nu_{pyridine}$ at each temperature were fitted to two peaks (Fig. 3f), in which one is assigned to the bonded hydrogen bonds, while the other is attributed to the free groups. Note that the peak of higher wavenumber is assigned to H-bonded pyridine due to its high sensitivity on protonation,[50] whereas the peak having reduced wavenumber belongs to H-bonded C=O. Their respective content is calculated according to the peak areal integral. With an increase of the temperature from 25 to 125 °C, the contents of free carbamate groups increase from 54.90% to 64.30% accordingly. A similar observation arose from free pyridine groups, the content of which rises to 57.55% at 125 °C. These results suggest that more hydrogen bonding moieties may be dynamically bonded with the sandwiched interface at elevated temperatures, providing that the PUPDM/LM/Al_2O_3 composite had a higher adhesive strength when cooled down. As a result, the PUPDM/LM/Al_2O_3 composite exhibits a high lap shear strength of 1.50 MPa when it adheres to the sandwiched aluminium plates (Fig. 3g and Fig. S19a, ESI†), which is about 2-fold of the PUPDM/Al_2O_3 counterpart (0.72 MPa). However, the PUPDM/LM/Al_2O_3 composite adhesion force is still lower than that of the pristine PUPDM and PUPDM/LM composite. The former has the highest contact region for the pyridine and carbamate moieties to bind with the hydroxyl groups on the aluminum plate, while the latter exhibits a much smaller elastic

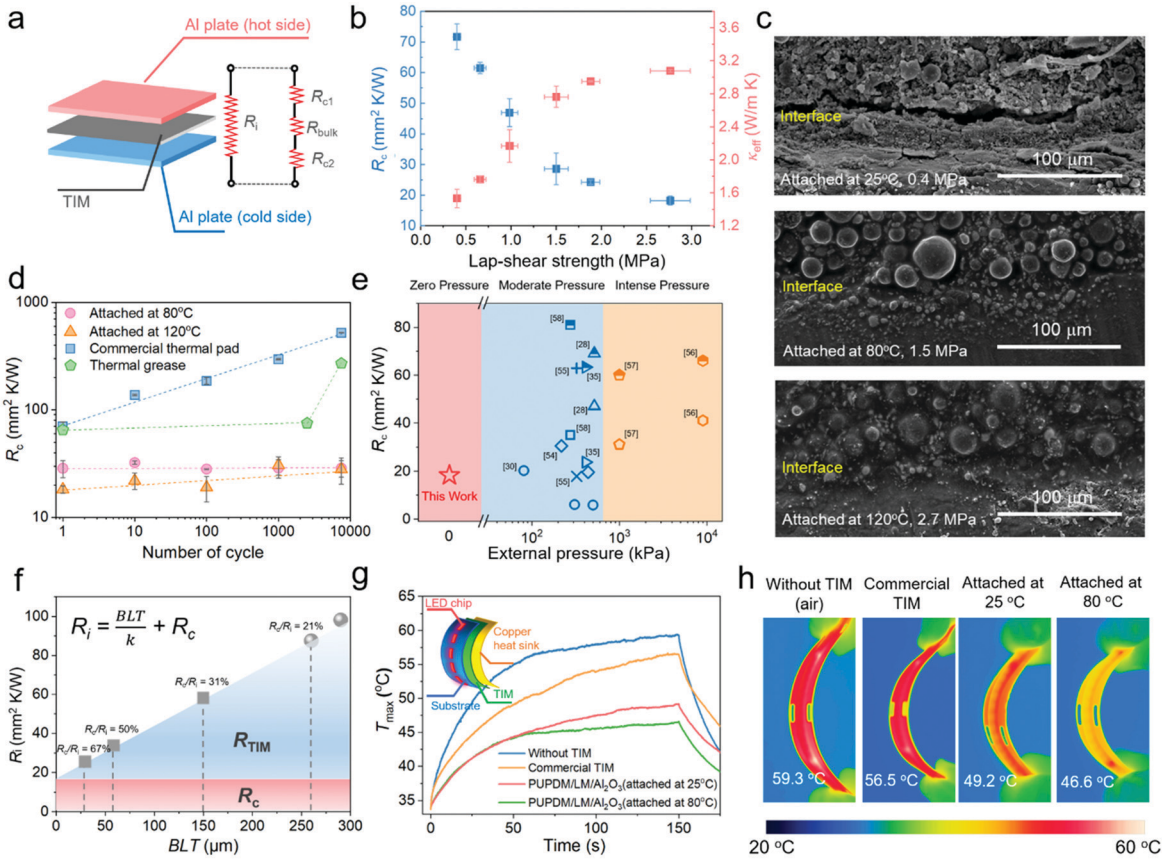

Fig. 4 Interfacial thermal management by employing the PUPDM/LM/Al_2O_3 composite. (a) Schematic illustration plotting the components in a sandwiched thermal interface. (b) Thermal contact resistance (two sides) and the effective thermal conductivity of the PUPDM/LM/Al_2O_3 composite TIM as a function of the lap-shear strength in the sandwiched smooth aluminum plates. (c) Scanning electron microscopy images of the microscopic interface between the PUPDM/LM/Al_2O_3 composite and the aluminum plates adhered at 25, 80, and 120 °C, respectively. (d) Thermal contact resistance (two sides) as a function of the number of times of cyclic heating and cooling for the PUPDM/LM/Al_2O_3 composites (adhered at 80 °C and 120 °C), a commercial TIM, and a thermal grease reported in the previous literature. (e) Comparison of the thermal contact resistance (two sides) of PUPDM/LM/Al_2O_3 composite TIM (adhered at 120 °C, no pressure) with those of reported TIMs in the literature or market. (f) The variation of the thermal contact resistance ratio to the total resistance of the thermal interface as a function of BLT. The circular points are experimental results, and the quadrate points are theoretically estimated values. (g) A schematic of the thermal management of a flexible light-emitting diode strip, with its working temperature with an increase of time. (h) The recorded infrared images of the flexible light-emitting diode strips after working for 150 s.

modulus that enables more efficient interfacial contact. Nevertheless, in consideration of both the thermo-conductive behaviour and the adhesive property, our PUPDM/LM/Al_2O_3 composite is the best candidate for TIM applications. Fig. 3h and Fig. S19b (ESI†), further demonstrate its universal adhesive function with regard to different polymer-based and metal-based substrates. Moreover, this highly sticky behaviour for the PUPDM/LM/Al_2O_3 composite is reversible because even after five times of cyclic adhesion and debonding, the sandwiched aluminium sheets bonded by the PUPDM/LM/Al_2O_3 adhesive can still lift a 10.66 kg bucket with minor adhesion changes (Fig. 3i). As discussed above, the reversible surface adhesive performance is expected to ensure reliable and durable heat conduction across the microscopic interface between the TIM and the heat sink or heat source.

2.4 Interfacial thermal management performance and application

The high thermal conductivities and robust and reversible interfacial adhesion were implemented for the PUPDM/LM/Al_2O_3 composite, which is expected to facilitate both the internal heat flux within the TIM and the interfacial heat propagation outside the TIM. In Fig. 4a, to simulate the heat dissipation across a sandwiched thermal interface, the PUPDM/LM/Al_2O_3 composite (73.68 vol%) serving as the TIM was adhered to two pieces of smooth aluminium plate. Its R_c and effective thermal conductivity (κ_{eff}) were qualified according to the following equations:

$$R = R_{Al} + R_i \quad (2)$$

$$R_i = R_{bulk} + R_c = BLT/\kappa_{eff} \quad (3)$$

$$R_{bulk} = BLT/\kappa_{TIM} \quad (4)$$

$$R_c = R_{c1} + R_{c2} \quad (5)$$

where R is the total thermal resistance of the sandwiched thermal interface, R_{Al} is the thermal resistance of aluminum plates at the hot side and cold side, R_i is the total resistance of

the interface between two aluminum plates, R_{bulk} is the intrinsic thermal resistance of the TIM, R_c is the thermal contact resistance between the TIM and the double sides, BLT is the bond line thickness, κ_{eff} is the effective thermal conductivity of a TIM, and κ_{TIM} is the intrinsic thermal conductivity of a TIM. The BLT of TIMs used for thermal property measurements were about 250 μm. More experimental details can be found in the ESI.† Since the lap-shear strength of the PUPDM/LM/Al_2O_3 composite is dependent on the handling temperature (Fig. S20, ESI†), we can adjust the adhesion of the sandwiched thermal interface to investigate its influence on the R_c and κ_{eff} of the thermal interface (Fig. 4b). With an increase of the lap-shear strength, the R_c gradually reduces, while the κ_{eff} increases. The minimum R_c could approach 18.28 mm^2 K W^{-1} under zero pressure, and its κ_{eff} (3.08 W m K^{-1}) could preserve 70% of the inherent κ of TIM (4.38 W m K^{-1}). The remarkable reduction in R_c partially results from the elimination of the interfacial air gaps and voids (Fig. 4c). However, when the lap-shear strength exceeds 1.5 MPa, the double sides of the thermal interface are well bonded without any visual grooves and valleys observed from the SEM images. The trend in R_c or κ_{eff} exactly presents a turning point in this situation. We assume that in addition to the removal of the interfacial air gaps, the high hydrogen bonding at the contact interface could stepwise promote the heat conduction *via* the intermolecular non-covalent interactions.[33,51,52] Meanwhile, a corrosion test was conducted to demonstrate the anticorrosion characteristic of our PUPDM/LM/Al_2O_3 composite, proving no reaction between aluminum and gallium in our composite (Fig. S21 and S22, ESI†).[53] Therefore, a prominently low R_c without applying any pressure was achieved for our PUPDM/LM/Al_2O_3 composite, while traditional TIMs adapting just the surface conformation could not. The double surfaces of the thermal interface more or less have a certain roughness under an actual situation. Therefore, we also designed the aluminum plates with a few patterns to conduct similar experiments (Fig. S23, ESI†), which demonstrates the identical effectiveness of the PUPDM/LM/Al_2O_3 TIM in the interfacial thermal management for some rough substrates.

Traditional TIMs usually behave with a noticeable R_c deterioration because of the thermal expansion coefficient mismatch with other electronic components. For example, a commercial thermal pad (4 W m K^{-1}) with good adhesive strength to the sandwiched aluminum substrates suffers from 6.5 times R_c improvement after long-term service (Fig. 4d). A similar phenomenon (3.2-fold R_c) was also observed in a previously reported thermal grease after 7500 cyclic heating and cooling times.[29] However, attributed to the dynamic and reversible interfacial hydrogen bonds at the sandwiched thermal interface, our PUPDM/LM/Al_2O_3 composite TIM manifests a negligible increment in R_c, which paves the way for the state-of-the-art thermal management of advanced electronics, and guarantees them valid and long-term service. More importantly, external packing pressure is necessary for TIMs in the literature and market to increase the actual contact area and enhance the interfacial thermal transport, thus adding complications to actual applications.[31] Owing to the adhesive nature, our PUPDM/LM/Al_2O_3 composite TIM shows much lower R_c (two sides) under zero pressure when compared with other reported TIMs that require moderate packing pressure (<650 kPa) or intense packing pressure (>1 MPa) (Fig. 4e and Table S5, ESI†).[28,30,35,54–58] In Fig. 4f, we signify that R_c would dominate the total resistance of the thermal interface with the rapid miniaturization of electronic devices. For example, when BLT gets less than 50 μm, our experimental result suggests that R_c will occupy more than 50% of the total thermal resistance. For the thermal management of such a micron thermal interface, the concept of a designed surface adhesion property will become more indispensable.

As mentioned above, the exquisite combination of high thermal conductivity yet electrical insulation, reversible adhesive ability, and good softness make this PUPDM/LM/Al_2O_3 composite a promising candidate for the next-generation TIMs applied in cutting-edge fields, such as wearable electronics, soft robotics, and flexible devices. Herein, taking a flexible light-emitting diode (LED) strip as a proof-of-concept, we employed our PUPDM/LM/Al_2O_3 composite (73.68 vol%, 250 μm) as the TIM and copper foil as the heat sink (Fig. 4g). The integrated LED device was bent, and its thermal management performance was evaluated by thermal imaging technology (Fig. 4g-h). For comparison, one commercial thermal pad (250 μm) and direct surface-to-surface contact were also considered. The surface temperature of the LED strip was recorded after different working times. Our PUPDM/LM/Al_2O_3 composite exhibits outstanding heat-dissipation capability as its surface temperature exhibits the lowest heating rate. Moreover, the higher interfacial hydrogen bonding also promotes cross-interface heat conduction. The LED managed by the PUPDM/LM/Al_2O_3 composite adhered at 80 °C keeps a much lower working temperature than that adhered at 25 °C.

3 Conclusions

In summary, we have reported a highly thermo-conductive, electrically insulating, and reversibly adhesive PUPDM/LM/Al_2O_3 composite. The exquisite TIM manifests a high thermal conductivity reaching 6.23 W m^{-1} K^{-1} when loaded with 82.76 vol% LM/Al_2O_3 content and allows a rapid and isotropic heat dissipation within the bulk material. In addition, the dynamic and reversible adhesion in this composite TIM also offers a low R_c value of only 18.28 mm^2 K W^{-1} when sandwiched between double aluminum plates under zero pressure, promising effective cross-interface heat conduction outside the TIM. More importantly, despite the serious mismatch in thermal expansion coefficient between our PUPDM/LM/Al_2O_3 composite and the aluminum substrate, this thermal pad integrating the advantages of reversible hydrogen bonding and high thermal conductivities manifests valid and durable thermal transport across a macro interface, even after 7500 cyclic heating and cooling processes. This new concept of constructing dynamic and reversible intermolecular interactions between the high-thermal-conductivity TIM and the double sides of the thermal interface will impact applications including microelectronic cooling, thermoelectric energy collection, and powerful wearables.

Author contributions

K. Wu initiated and designed the experiments. K. Wu and Q. Fu supervised the experiments. C. Guo and Y. H. Li fabricated the materials and performed the experimental tests. K. Wu and C. Guo wrote the manuscript. K. Wu, C. Guo, J. H. Xu and Q. Fu analyzed the data. All the authors contributed to the scientific discussion.

Conflicts of interest

There are no conflicts to declare.

Acknowledgements

This work was financially supported by the National Natural Science Foundation of China (Grant No. 52103091, 51573102 and 51421061) and the Natural Science Foundation of Jiangsu Province (Grant No. BK20200501). We also appreciate Hui Wang from the Analytical & Testing Center of Sichuan University for her help with SEM characterization.

Notes and references

1 A. L. Moore and L. Shi, *Mater. Today*, 2014, **17**, 163–174.
2 M. M. Waldrop, *Nature*, 2016, **530**, 144–148.
3 P. Ball, *Nat. News*, 2012, **492**, 174.
4 J. S. Kang, M. Li, H. Wu, H. Nguyen and Y. Hu, *Science*, 2018, **361**, 575–578.
5 C. Lei, Z. Xie, K. Wu and Q. Fu, *Adv. Mater.*, 2021, 2103495.
6 K. Wu, C. Lei, R. Huang, W. Yang, S. Chai, C. Geng, F. Chen and Q. Fu, *ACS Appl. Mater. Interfaces*, 2017, **9**, 7637–7647.
7 H. Guo, H. Zhao, H. Niu, Y. Ren, H. Fang, X. Fang, R. Lv, M. Maqbool and S. Bai, *ACS Nano*, 2021, **15**, 6917–6928.
8 D. Liu, C. Lei, K. Wu and Q. Fu, *ACS Nano*, 2020, **14**, 15738–15747.
9 X. Zeng, J. Sun, Y. Yao, R. Sun, J. B. Xu and C. P. Wong, *ACS Nano*, 2017, **11**, 5167–5178.
10 Y. Zhang, C. Lei, K. Wu and Q. Fu, *Adv. Sci.*, 2021, **8**, 2004821.
11 J. Chen, X. Huang, Y. Zhu and P. Jiang, *Adv. Funct. Mater.*, 2017, **27**, 1604754.
12 P. Min, J. Liu, X. Li, F. An, P. Liu, Y. Shen, N. Koratkar and Z.-Z. Yu, *Adv. Funct. Mater.*, 2018, **28**, 1806365.
13 M. Qin, Y. Xu, R. Cao, W. Feng and L. Chen, *Adv. Funct. Mater.*, 2018, **28**, 1805053.
14 Y. Zhang, K. Wu and Q. Fu, *Adv. Funct. Mater.*, 2021, 202109255.
15 A. Yu, P. Ramesh, X. Sun, E. Bekyarova, M. E. Itkis and R. C. Haddon, *Adv. Mater.*, 2008, **20**, 4740–4744.
16 P. Song, B. Liu, C. Liang, K. Ruan, H. Qiu, Z. Ma, Y. Guo and J. Gu, *Nanomicro Lett.*, 2021, **13**, 91.
17 X. Zeng, Y. Yao, Z. Gong, F. Wang, R. Sun, J. Xu and C. P. Wong, *Small*, 2015, **11**, 6205–6213.
18 N. Kazem, T. Hellebrekers and C. Majidi, *Adv. Mater.*, 2017, **29**, 1605985.
19 S. Chen, H.-Z. Wang, R.-Q. Zhao, W. Rao and J. Liu, *Matter*, 2020, **2**, 1446–1480.
20 M. D. Bartlett, N. Kazem, M. J. Powell-Palm, X. Huang, W. Sun, J. A. Malen and C. Majidi, *Proc. Natl. Acad. Sci. U. S. A.*, 2017, **114**, 2143–2148.
21 S. Mei, Y. Gao, Z. Deng and J. Liu, *J. Electron. Packaging*, 2014, **136**, 011009.
22 A. B. M. T. Haque, R. Tutika, R. L. Byrum and M. D. Bartlett, *Adv. Funct. Mater.*, 2020, **30**, 2000832.
23 D. Yu, Y. Liao, Y. Song, S. Wang, H. Wan, Y. Zeng, T. Yin, W. Yang and Z. He, *Adv. Sci.*, 2020, **7**, 2000177.
24 D. Wang, D. Liu, J. Xu, J. Fu and K. Wu, *Mater. Horiz.*, 2022, **9**, 640–652.
25 P. Fan, Z. Sun, Y. Wang, H. Chang, P. Zhang, S. Yao, C. Lu, W. Rao and J. Liu, *RSC Adv.*, 2018, **8**, 16232–16242.
26 H. Wang, W. Xing, S. Chen, C. Song, M. D. Dickey and T. Deng, *Adv. Mater.*, 2021, **33**, 2103104.
27 R. Tutika, S. H. Zhou, R. E. Napolitano and M. D. Bartlett, *Adv. Funct. Mater.*, 2018, **28**, 1804336.
28 W. Dai, L. Lv, J. Lu, H. Hou, Q. Yan, F. E. Alam, Y. Li, X. Zeng, J. Yu, Q. Wei, X. Xu, J. Wu, N. Jiang, S. Du, R. Sun, J. Xu, C.-P. Wong and C.-T. Lin, *ACS Nano*, 2019, **13**, 1547–1554.
29 K. C. Otiaba, N. N. Ekere, R. S. Bhatti, S. Mallik, M. O. Alam and E. H. Amalu, *Microelectron. Reliab.*, 2011, **51**, 2031–2043.
30 W. Dai, T. Ma, Q. Yan, J. Gao, X. Tan, L. Lv, H. Hou, Q. Wei, J. Yu and J. Wu, *ACS Nano*, 2019, **13**, 11561–11571.
31 M. Seong, I. Hwang, S. Park, H. Jang, G. Choi, J. Kim, S. K. Kim, G. H. Kim, J. Yeo and H. E. Jeong, *Adv. Funct. Mater.*, 2021, **31**, 2107023.
32 K. Zheng, F. Sun, J. Zhu, Y. Ma, X. Li, D. Tang, F. Wang and X. Wang, *ACS Nano*, 2016, **10**, 7792–7798.
33 F. Sun, T. Zhang, M. M. Jobbins, Z. Guo, X. Zhang, Z. Zheng, D. Tang, S. Ptasinska and T. Luo, *Adv. Mater.*, 2014, **26**, 6093–6099.
34 M. D. Losego, M. E. Grady, N. R. Sottos, D. G. Cahill and P. V. Braun, *Nat. Mater.*, 2012, **11**, 502–506.
35 Q. Yan, F. E. Alam, J. Gao, W. Dai, X. Tan, L. Lv, J. Wang, H. Zhang, D. Chen and K. Nishimura, *Adv. Funct. Mater.*, 2021, **31**, 2104062.
36 H. Yu, Y. Feng, C. Chen, Z. Zhang, Y. Cai, M. Qin and W. Feng, *Carbon*, 2021, **179**, 348–357.
37 M. Wang, T. Li, Y. Yao, H. Lu, Q. Li, M. Chen and Q. Li, *J. Am. Chem. Soc.*, 2014, **136**, 18156–18162.
38 Q. Ngo, B. A. Cruden, A. M. Cassell, G. Sims, M. Meyyappan, J. Li and C. Y. Yang, *Nano Lett.*, 2004, **4**, 2403–2407.
39 V. Singh, T. L. Bougher, A. Weathers, Y. Cai, K. Bi, M. T. Pettes, S. A. McMenamin, W. Lv, D. P. Resler and T. R. Gattuso, *Nat. Nanotechnol.*, 2014, **9**, 384–390.
40 S. M. Kim, H. Jeon, S. H. Shin, S. A. Park, J. Jegal, S. Y. Hwang, D. X. Oh and J. Park, *Adv. Mater.*, 2018, **30**, 1705145.
41 Z. Xu, L. Chen, L. Lu, R. Du, W. Ma, Y. Cai, X. An, H. Wu, Q. Luo and Q. Xu, *Adv. Funct. Mater.*, 2021, **31**, 2006432.
42 Y. Yao, Z. Xu, B. Liu, M. Xiao, J. Yang and W. Liu, *Adv. Funct. Mater.*, 2021, **31**, 2006944.

43 Y. Li, W. Li, A. Sun, M. Jing, X. Liu, L. Wei, K. Wu and Q. Fu, *Mater. Horiz.*, 2021, **8**, 267–275.
44 K. Wu, D. Liu, C. Lei, S. Xue and Q. Fu, *Chem. Eng. J.*, 2020, **394**, 124929.
45 Z. Wu, C. Xu, C. Ma, Z. Liu, H. M. Cheng and W. Ren, *Adv. Mater.*, 2019, **31**, 1900199.
46 S. Y. Pak, H. M. Kim, S. Y. Kim and J. R. Youn, *Carbon*, 2012, **50**, 4830–4838.
47 J. Che, K. Wu, Y. Lin, K. Wang and Q. Fu, *Composites, Part A*, 2017, **99**, 32–40.
48 W. Yu, H. Xie, L. Yin, J. Zhao, L. Xia and L. Chen, *Int. J. Therm. Sci.*, 2015, **91**, 76–82.
49 C.-W. Nan, R. Birringer, D. R. Clarke and H. Gleiter, *J. Appl. Phys.*, 1997, **81**, 6692–6699.
50 V. Balevicius, R. Bariseviciute, K. Aidas, I. Svoboda, H. Ehrenberg and H. Fuess, *Phys. Chem. Chem. Phys.*, 2007, **9**, 3181–3189.
51 J. H. Taphouse, O. N. L. Smith, S. R. Marder and B. A. Cola, *Adv. Funct. Mater.*, 2014, **24**, 465–471.
52 G.-H. Kim, D. Lee, A. Shanker, L. Shao, M. S. Kwon, D. Gidley, J. Kim and K. P. Pipe, *Nat. Mater.*, 2015, **14**, 295–300.
53 Y.-G. Deng and J. Liu, *Appl. Phys. A: Mater. Sci. Process.*, 2009, **95**, 907–915.
54 L. Ping, P.-X. Hou, H. Wang, M. Chen, Y. Zhao, H. Cong, C. Liu and H.-M. Cheng, *Carbon*, 2018, **133**, 275–282.
55 J. Gao, Q. Yan, L. Lv, X. Tan, J. Ying, K. Yang, J. Yu, S. Du, Q. Wei, R. Xiang, Y. Yao, X. Zeng, R. Sun, C.-P. Wong, N. Jiang, C.-T. Lin and W. Dai, *Chem. Eng. J.*, 2021, **419**, 129609.
56 X. Tan, J. Ying, J. Gao, Q. Yan, L. Lv, K. Nishimura, Q. Wei, H. Li, S. Du, B. Wu, R. Xiang, J. Yu, N. Jiang, C.-T. Lin and W. Dai, *Compos. Commun.*, 2021, **24**, 100621.
57 P. Zhang, Q. Li and Y. Xuan, *Composites, Part A*, 2014, **57**, 1–7.
58 H. Chen, M. Chen, J. Di, G. Xu, H. Li and Q. Li, *J. Phys. Chem. C*, 2012, **116**, 3903–3909.